Unsteady Panel Method for Complex Configurations Including Wake Modeling

Louw H. van Zyl*

Council for Scientific and Industrial Research, Pretoria 0001, South Africa

The calculation of unsteady air loads is an essential step in any aeroelastic analysis. The subsonic doublet lattice method is used extensively for this purpose because of its simplicity and reliability. The body models available with the popular implementations of the doublet lattice method are, however, not very versatile in terms of geometries that can be modeled. The ZONA6 code offers a versatile surface panel body model including a separated wake model, but uses a pressure panel method for lifting surfaces. This paper describes the development of an unsteady subsonic wing–body code based on the doublet lattice method, with a source panel representation of bodies, a separated wake flow model based on the ZONA6 approach, and an approximate method of images to model wing–body interference. This approach provides greater flexibility in body shapes that can be modeled while retaining the reliability of the doublet lattice method for lifting surfaces.

Nomenclature

a_∞ = speed of sound in undisturbed air
C_p = pressure coefficient
C_p^0 = steady pressure coefficient
C_p^1 = unsteady pressure coefficient
C_{pb}^0 = steady base pressure coefficient
C_{pb}^1 = unsteady base pressure coefficient
$\boldsymbol{h}$ = modal displacement vector
I_0 = $\int_{s_1}^\infty \frac{e^{-\omega_r s}}{(r^2+s^2)^{1/2}}\,ds$
K_1 = planar part of the kernel function, $r(\partial I_0/\partial r)$
M_∞ = freestream Mach number
$\boldsymbol{n}$ = instantaneous normal vector, $\boldsymbol{n}_0 + \boldsymbol{r}e^{i\omega t} \times \boldsymbol{n}_0$
$\boldsymbol{n}_0$ = mean normal vector
R = $\sqrt{x^2 + \beta^2 r^2}$
r = radial coordinate, $\sqrt{y^2 + z^2}$
$\boldsymbol{r}$ = modal rotation vector
s_1 = $\frac{MR-x}{\beta^2}$
U = freestream velocity magnitude
u = streamwise plunge velocity
$\boldsymbol{u}$ = instantaneous total velocity vector, $\boldsymbol{u}_\infty + \boldsymbol{u}_0 + \boldsymbol{u}_1 e^{i\omega t}$
$\boldsymbol{u}_0$ = steady perturbation velocity vector
$\boldsymbol{u}_1$ = unsteady perturbation velocity vector
$\boldsymbol{u}_\infty$ = freestream velocity vector
x = chordwise coordinate
y = spanwise coordinate
z = vertical coordinate
β = $\sqrt{1 - M_\infty^2}$
γ = ratio of specific heats
ρ^0 = steady local density
Φ = total velocity potential, $\phi + \varphi e^{i\omega t}$
ϕ = steady velocity potential
φ = unsteady velocity potential
ω = angular velocity
ω_r = wave number, $i\omega/U$

Introduction

THE subsonic doublet lattice method (DLM) [1] has been the workhorse of aeroelastic analysis for several decades. The body

*Engineer, Aeronautic Systems, Post Office Box 395.

models that are available for the H7WC/N5KA/N5KQ [2–4] family of codes are, however, limited to the slender body/interference panel method and the method of images. Slender body theory is an effective way of modeling the flow about isolated axially symmetric bodies in both steady and unsteady flow. The vortex lattice method (VLM) and the DLM are effective methods of modeling steady and unsteady flows about lifting surfaces. In the case of wing–body combinations, the circulatory flow about the lifting surfaces distorts the flow around the body to such an extent that slender body theory becomes inadequate to model the flow about the body in the region of the wing–body junction. On a macro scale, the velocity induced by the lifting surface at the body surface in a section through the body is not constant, which violates the assumptions of slender body theory. On a micro scale, the lifting lines that end at the body surface and are not perpendicular to the surface induce large velocities normal to the body surface.

The solution to this problem implemented in the H7WC code is to place lifting surface panels on an idealized body of constant cross-sectional shape. Slender body theory (i.e., axial pressure doublets in unsteady flow), is still used to model the flow around the isolated body, whereas the lifting surface elements cancel the nonuniform velocities induced by the lifting surfaces of the configuration. One drawback of this method is that each lifting surface panel used to model the wing–body interference introduces another unknown into the downwash equation.

The method of images was implemented in the N5KA code by directly replacing the steady vortex lattice on lifting surfaces and image surfaces by an unsteady vortex lattice (i.e., an unsteady pressure doublet lattice). The combination of a trailing vortex and its image within a cylindrical body produces a constant induced velocity around the body circumference. In addition, the image of the bound vortex or doublet line at the junction of the vortex line and the body surface cancels the large normal velocities induced by the bound vortex. No new unknowns are introduced in the downwash equation. The same method is used in the N5KQ code with its refined lifting surface model.

In the early 1970s the National Aerospace Laboratory of the Netherlands (NLR) undertook an extensive research program to investigate unsteady airloads on oscillating wing-store configurations. This effort culminated in the NLRS method for solving the steady flowfield and the NLRI method for solving the combined steady and unsteady flowfield. Roos et al. employed a surface panel body model in the NLRI method [5]. Slender body theory is not used at all, and the body is represented by source panels on the actual or idealized body surface. Although the limitation of constant velocity in a cross section of slender body theory no longer applies, a simplified method of images is still used in this method to solve the

problem of large induced normal velocities at the wing–body junction and to move the trailing vortex to the body axis. Several more advanced methods for calculating the unsteady flow about complex configurations in subsonic and supersonic flow were developed at NLR by Hounjet [6–8]. These methods can model both thin lifting surfaces similar to those in the DLM and lifting bodies (i.e., lifting surfaces with the full profile defined). The singularities and solution methods employed in these methods are quite different from those employed in the DLM and are beyond the scope of the present work.

The ZONA6 code [9] offers a surface panel body model including wake effect. The wake model has an effect on the axial flow as well as the crossflow. In axial flow, the velocity, and consequently the pressure over the rear of a blunt-tailed body, is modified by the wake closure condition. In crossflow, the pressure around the edge of the base is equalized through the wake flow region, resulting in the lateral loading going to zero at the base. The merits of the pressure panel method used in ZONA6 for modeling lifting surfaces are, however, disputed [10,11].

The present method employs the DLM for lifting surfaces and a surface panel body model that is similar to the NLRI method of Roos et al. It is an extension to the NLRI method in three aspects. First, it avoids the calculation of higher-order derivatives of the steady disturbance potential to obtain the coupling between the steady and the superimposed unsteady flowfields. This reduces the complexity of the method significantly and results in an acceptable approximation.

The second extension involves the use of a two-strip image model. The first strip creates a high-fidelity image in the immediate vicinity of the doublet line/body surface intersection, whereas the second strip moves the trailing vortex to a suitable location, typically a body centerline. The high-fidelity image, which is defined by the user and should follow the rules of the classical method of images, reduces the normal velocity induced by unsteady doublet lines or steady horseshoe vortices on the body surface. It is therefore not necessary to refine the body paneling in the wing–body junction region excessively. This method makes it easier to model the wing–body junction on a body with an irregular cross section, or in cases in which the wing does not join the body in a radial direction.

The third extension concerns the wake flow of a blunt-based body and is similar to the model used in ZONA6. Viewed from a distance, a body that does not contain a propulsion unit should be neither a source nor a sink. In the case of a body with a pointed tail, this condition is approximately satisfied by enforcing the boundary conditions. However, in the case of a blunt-based body, this is not the case if the base is not paneled. On the other hand, paneling the base of the body would erroneously enforce attached potential flow over the base. A point source of unknown strength, placed in the wake of the body, is used in the present method to enforce the condition of zero total source strength. A doublet in the wake region is used to enforce the condition of zero loading at the base as well as a specified base pressure, if specified. The solution of the steady flowfield is necessarily an iterative process because of the nonlinear expression for pressure used in the steady flow; however, convergence is rapid, and only a few iterations are needed. Similar conditions are enforced on the unsteady flowfield. If a steady base pressure is specified, the unsteady base pressure is derived from the steady base pressure and the streamwise motion of the body. If a base pressure is not specified, the steady and the unsteady condition is that the axial component of the doublet is zero. Because of the linearization of the expression for unsteady pressure, no iteration is required in the unsteady case.

Theory

Governing Equations and Elementary Solutions

The basis of the analysis is the linearized small disturbance equation, viz.

$$\left(1 - M_\infty^2\right)\Phi_{xx} + \Phi_{yy} + \Phi_{zz} - 2\frac{M_\infty}{a_\infty}\Phi_{xt} - \frac{1}{a_\infty^2}\Phi_{tt} = 0 \quad (1)$$

The steady and unsteady parts of the velocity potential satisfy the Prandtl–Glauert equation

$$\left(1 - M_\infty^2\right)\phi_{xx} + \phi_{yy} + \phi_{zz} = 0 \quad (2)$$

and the linearized small disturbance equation

$$\left(1 - M_\infty^2\right)\varphi_{xx} + \varphi_{yy} + \varphi_{zz} - 2M_\infty^2\omega_r\varphi_x - M_\infty^2\omega_r^2\varphi = 0 \quad (3)$$

respectively. The basic steady solutions are steady sources and horseshoe vortices as used in the vortex lattice method. The basic unsteady solutions are unsteady sources and acceleration potential doublet lines as used in the DLM.

Wake Model

In the ZONA6 code [9], a base pressure and the positions of a steady source and an unsteady doublet in the wake are specified. The source and doublet strengths are determined to give the required steady base pressure and zero unsteady pressure on the body surface panels adjacent to the base. Wake closure is ensured implicitly, resulting in a realistic wake shape.

In the present method, a steady source and doublet are employed to enforce the steady wake conditions, and an unsteady source and doublet are employed to enforce the unsteady wake conditions. The positions of the steady and unsteady sources and the positions of the steady and unsteady doublets coincide, but the sources and doublets are generally not colocated. The doublets are placed close to the base of the body, whereas the sources are placed farther downstream. The positions of the source and the doublet in the wake are specified by the user and a base pressure may also be specified. The wake conditions are as follows:

1) The total source strength of the body surface panels and the point source in the wake must be zero.

2) The z loading must be zero over the last segment of the body.

3) The y loading must be zero over the last segment of the body.

4) The steady base pressure must be equal to the specified value, and the unsteady base pressure must be equal to a corresponding value derived from the steady base pressure and the streamwise motion of the body, or the x component of the doublet must be zero.

The base pressure is calculated as the area-weighted average of the pressures on the panels of the last segment of the body. The area weighting is based on triangles formed by the centroid of the base and the trailing edges of the panels of the last segment of the body. The y and z loading are derived from the vector sum of the normal vectors times the pressure over the last segment of the body.

The unsteady base pressure may be significant for under-wing stores, in which case, a pitching motion of the wing will also lead to significant streamwise motion of the store. The unsteady base pressure is calculated, and the motion of the base centroid is determined for each mode. The base is then treated as a physical panel in the calculation of generalized forces. In contrast, the ZONA6 code enforces a zero unsteady base pressure.

In the case of a tip store, the wing-tip trailing vortex emanates from the base of the store. The interaction between the steady and unsteady trailing vortices, or the unsteady trailing vortex by itself, may induce significant unsteady pressures on the rear of the body. Also, in this case, it may be unrealistic to enforce a zero unsteady base pressure even though the unsteady base pressure does not contribute to the generalized forces.

Induced Potential, Velocity, and Pressure

The induced velocity potential of an unsteady point source is given by

$$\varphi = \frac{-1}{4\pi R}\exp\left(\frac{\omega_r M_\infty}{\beta^2}(M_\infty x - R)\right) \quad (4)$$

The induced velocities are given by the derivatives of the velocity potential in a given direction. Corresponding expressions for the steady source can easily be derived from the expressions for the

unsteady source and are not presented here.

$$\varphi_x = -\varphi \left\{ \frac{x}{R^2} - \frac{\omega_r M_\infty}{\beta^2} \left(M_\infty - \frac{x}{R} \right) \right\} \tag{5}$$

$$\varphi_y = -\varphi \left\{ \frac{\beta^2 y}{R^2} + \frac{\omega_r M_\infty y}{R} \right\} \tag{6}$$

$$\varphi_z = -\varphi \left\{ \frac{\beta^2 z}{R^2} + \frac{\omega_r M_\infty z}{R} \right\} \tag{7}$$

The steady induced potential and velocity of a source panel are calculated by analytical integration. To treat warped quadrilateral panels consistently, all quadrilateral panels are approximated by four triangular panels, each with the collocation point of the panel as apex and one side of the panel as base. The analytical integration is therefore always performed over flat triangular panels.

The unsteady induced potential and velocity of a source panel are calculated by subtracting the steady part of the integrand, integrating the remainder using Gaussian quadrature, and adding the analytical integral of the steady part. In this way, the integration error is minimized whereas the analytical integration only needs to be performed once for each Mach number/angle-of-attack combination. The isoparametric formulation, which is widely used in finite element analysis, is also used here for the numerical integration of the unsteady parts. In this formulation, the physical, possibly warped, panel is mapped to a flat rectangular panel through shape functions that depend only on the panel corner point coordinates. In the case of warped quadrilateral panels, there will be a small discrepancy between the isoparametric representation of the panel used for the integration of the unsteady part and the plane triangle approximation used for the analytical integration of the steady part.

In the DLM for lifting surfaces, only the induced velocity normal to a receiving panel aligned with the freestream is calculated as the influence coefficient, and the pressure difference over the lifting surface is solved directly from the downwash equation. In the present wing–body code, the more general boundary condition requires the full unsteady velocity vector induced by a doublet line to be calculated, and the calculation of pressures on the body surface requires both the velocity vector and the induced potential. The y and z components of the velocity vector can easily be obtained from the usual downwash expressions by manipulating the direction cosine functions, which leaves the induced velocity in the x direction and the induced potential to be evaluated.

The velocity potential of an acceleration potential doublet line with strength corresponding to unit ΔC_p is given by (symbols have the meaning as defined in [2] except that the definition of ω_r has been substituted)

$$\varphi = \frac{\Delta x_s}{8\pi} \int_{-e}^{e} \frac{\bar{z}}{r} \frac{\partial I_0}{\partial r} \exp[-\omega_r(x_0 - \bar{\eta} \tan \lambda_s)] \, d\bar{\eta} \tag{8}$$

The expression for the potential induced by the doublet line can be written in terms of the kernel function as

$$\varphi = \frac{\Delta x_s}{8\pi} \int_{-e}^{e} \frac{\bar{z}}{r^2} K_1 \exp[-\omega_r(x_0 - \bar{\eta} \tan \lambda_s)] \, d\bar{\eta} \tag{9}$$

and the induced velocity in the x direction as

$$\varphi_x = \frac{\Delta x_s}{8\pi} \int_{-e}^{e} \frac{\bar{z}}{r^2} \frac{\partial}{\partial x_0} (K_1 \exp[-\omega_r(x_0 - \bar{\eta} \tan \lambda_s)]) \, d\bar{\eta}$$

$$= \frac{\Delta x_s}{8\pi} \int_{-e}^{e} \frac{\bar{z}}{r^2} \left(\frac{\partial K_1}{\partial x_0} - \omega_r K_1 \right) \exp[-\omega_r(x_0 - \bar{\eta} \tan \lambda_s)] \, d\bar{\eta} \tag{10}$$

Both these expressions are evaluated in the same way as the expressions for induced normal velocity (i.e., by curve fitting

followed by analytical integration). The steady parts are also evaluated analytically.

As in [5], the steady pressure coefficient on the body surface is calculated in the present method using the isentropic formula

$$C_p^0 = -\frac{2(\rho^{0\gamma} - 1)}{\gamma M_\infty^2} \tag{11}$$

and the unsteady pressure coefficient using the linear isentropic formula

$$C_p^1 = -2\rho^0(\phi_x \varphi_x + \phi_y \varphi_y + \phi_z \varphi_z + \omega_r \varphi) \tag{12}$$

As it stands, Eq. (12) applies to a stationary boundary. For a moving boundary, the changing local velocity because of the motion of the boundary must be taken into account. An extended expression for the unsteady pressure coefficient is given in the appendix of [5], in which the unsteady velocity because of the movement of the boundary is expressed as the product of the boundary displacement and the gradient of the steady disturbance velocity. The approach taken here is to consider a body in rigid motion. The steady singularity distribution representing the body, as well as the steady disturbance flowfield, moves with the body. This argument does not hold for elastic deformations; however, for a continuously deforming structure, the error introduced is attenuated by distance. The unsteady velocity because of the body motion is given by the rotation of the steady disturbance velocity vector, $r \times u_0$. The velocity of the boundary also introduces an unsteady potential. This term is given by the scalar product of the boundary velocity and the gradient of the steady potential (i.e., u_0). The result is a relatively simple expression for the unsteady pressure on the body surface that does not involve the gradient of the steady disturbance velocity.

$$C_p^1 = -2\rho^0[(u_\infty + u_0) \cdot u_1 + \omega_r \varphi + u_\infty \cdot (r \times u_0) - \omega_r h \cdot u_0] \tag{13}$$

This expression can be shown to yield unsteady pressures at zero frequency that are consistent with quasi-steady pressures for any rigid body motion.

The local density ratio in Eqs. (11–13) is given by

$$\rho^0 = \left(1 + \frac{\gamma - 1}{2} M_\infty^2 \left(1 - \phi_x^2 - \phi_y^2 - \phi_z^2 \right) \right) \tag{14}$$

Equations (11) and (13) are used to determine the pressures on body panels only. For lifting surface panels, the pressure differential is given directly by the local singularity strength.

Boundary Conditions

Steady boundary values for lifting surfaces can include angle of attack, incidence relative to the global coordinate axes, camber, and control surface deflections. Steady boundary conditions for bodies take account of angle-of-attack and body-axis incidence. Incidence, camber and control deflections are modeled by rotating the normal vectors only, without displacing corner or collocation points of panels.

A more general form of the boundary conditions than that of the standard DLM is used, and the same expression is used for lifting surfaces and bodies. The general form of the boundary condition is

$$\dot{h} \cdot n = u \cdot n \tag{15}$$

or

$$i\omega h e^{i\omega t} \cdot (n_0 + r \times n_0 e^{i\omega t})$$
$$= (u_\infty + u_0 + (h \cdot \nabla)u_0 e^{i\omega t} + u_1 e^{i\omega t}) \cdot (n_0 + r \times n_0 e^{i\omega t}) \tag{16}$$

It is assumed here that the rotation of the surface at the collocation point is known explicitly, resulting in a slightly simpler expression than in [5]. The steady boundary condition is

$$u_0 \cdot n_0 = -u_\infty \cdot n_0 \qquad (17)$$

and the unsteady boundary condition, neglecting higher order terms, is

$$i\omega h \cdot n_0 = (u_\infty + u_0) \cdot (r \times n_0) + (h \cdot \nabla)u_0 \cdot n_0 + u_1 \cdot n \quad (18)$$

or

$$u_1 \cdot n_0 = i\omega h \cdot n_0 - u_\infty \cdot (r \times n_0) - u_0 \cdot (r \times n_0)$$
$$- (h \cdot \nabla)u_0 \cdot n_0 \qquad (19)$$

The last term of Eq. (19) can lead to numerical problems, and the corresponding term was omitted in [16]. Nevertheless, good agreement was found between some, but not all, of the experimental and the calculated results. By the same reasoning used here, concerning the calculation of unsteady pressures (i.e., the steady disturbance flowfield moves with the body), the steady disturbance velocity does not contribute to the unsteady boundary condition in the case of rigid body motion. Therefore, the last two terms should be omitted for rigid body motions and not only the last one. This is done in the present method, accepting that elastic deformation introduces a small error. The unsteady boundary condition is therefore uncoupled from the steady disturbance flow.

Modal data for bodies is entered as the x, y, and z displacement and x, y, and z rotations of the body axis at each division. These values are interpolated to the collocation point x position on the axis and then transferred to the collocation point of each panel. Modal data for lifting surfaces is entered as the displacement and rotation at each box reference point. The values that are stored for each panel for each mode shape are $-u_\infty \cdot (r \times n_0)$ and $h \cdot n_0$ at the collocation point.

It is convenient to calculate the steady flow contribution to the unsteady pressure distribution over bodies at the same time as the boundary conditions:

$$C_p^1 = -2\rho^0[u_\infty \cdot (r \times u_0) - \omega_r h \cdot u_0] \qquad (20)$$

The values that are stored for each panel for each mode are $-2\rho^0 u_\infty \cdot (r \times u_0)$ and $2\rho^0 h \cdot u_0$ at the centroid. This contribution to the unsteady pressure on the last segment of the body also influences the wake conditions and is accounted for.

The unsteady base pressure is assumed to vary with the streamwise velocity of the base:

$$C_{pb}^1 = 2(i\omega h \cdot u_\infty/U)C_{pb}^0 \qquad (21)$$

where the steady base pressure in this case is the specified base pressure, and the modal displacement vector is taken at the base centroid.

Implementation

A computer code implementing the theory given here, excluding the wake model, is described in detail in [12]. Two major errors were, however, made in [12]: the third term in Eq. (19) was retained, and the last term in Eq. (13) was omitted.

The wake conditions are added to the downwash equation. Each body wake results in four unknowns being added (i.e., the source strength and the three components of the doublet). The equation for wake closure contains the area of each element of the body in the corresponding column and a 1 in the column corresponding to the source. The right-hand side is zero. The equation is identical for the steady and the unsteady cases.

The equation for the z loading contains for each singularity the sum of the products of the pressure induced by the singularity and the z component of the normal vector of each element in the last segment of the body. The right-hand side is zero. The equation for the y loading is similar, and the equations for steady and unsteady cases are similar except that the right-hand side in the unsteady case contains the loading resulting from the steady–unsteady flowfield coupling.

If a base pressure is specified, the equation for the base pressure contains for each singularity the sum of the products of the pressure induced by the singularity and the area of the triangle formed by the base centroid and the trailing edge of each element in the last segment of the body. The right-hand side is the specified base pressure times the base area in the steady case and the derived unsteady base pressure minus the unsteady pressure resulting from the steady–unsteady flowfield coupling, times the base area, in the unsteady case. If no base pressure is specified, the equation simply states that the x component of the doublet is zero.

For each wake singularity, a column is added to the downwash equation. These columns contain the downwash induced by the wake singularities at the lifting surface and body surface panel collocation points.

The nonlinear formula [Eq. (11)] used for the calculation of steady pressures in the wake conditions necessitates an iterative steady solution. The iterative process is formulated to determine the required incremental singularity distribution to eliminate the errors in the boundary conditions and the wake conditions. The starting condition is zero singularity strength, and therefore undisturbed flow, everywhere. The linearization used in the calculation of the unsteady pressures [Eq. (13)] is also used here. The iterative solution can therefore be regarded as a Newton–Rhapson procedure, and convergence is rapid.

Numerical Examples

Cone–Cylinder

Several aspects are investigated using the cone–cylinder studied by Bykov [13] as an example: positioning of the source in the wake, convergence of the steady solution, the behavior of the solution at the apex, the consistency between quasi-steady and zero-frequency unsteady solutions, and the effect of the wake model on the pitch-damping coefficient.

The nose of the cone–cylinder has an inclusive angle of 20 deg and $L/d = 7.5$. The conical section was initially divided into 8 segments and the cylindrical section into 14 segments. The nose segment was then repeatedly divided in two. This was done 10 times to obtain a nose segment with a length of $8.7 \times 10^{-5}d$ and a diameter of $1.5 \times 10^{-5}d$.

The steady base pressure is largely determined by the position of the source in the wake. The base pressure will approach the no-wake pressure when the source is placed far downstream. The base pressure will decrease as the source is moved closer to the base, as illustrated in Fig. 1. If the base pressure is known from experiment or a separate analysis, the axial position of the source should be adjusted to match the known base pressure reasonably well, without specifying the base pressure, before the base pressure value is specified. If the base pressure is not known, the streamlines and velocity vectors in the base region can be plotted to ensure that the
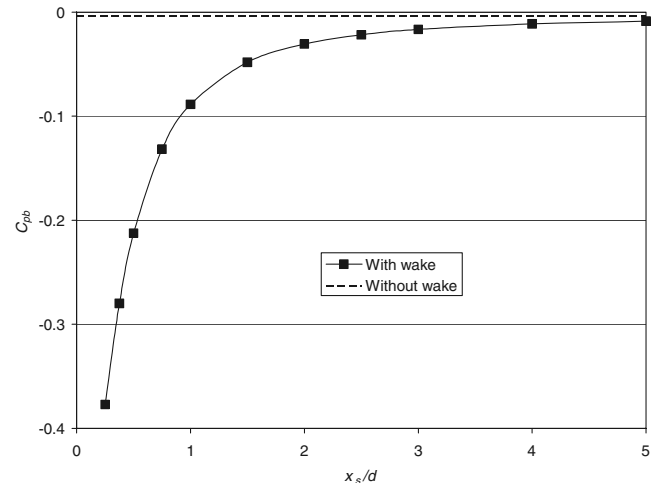

Fig. 1   Base pressure of the cone–cylinder in axial flow as a function of source position downstream of the base.
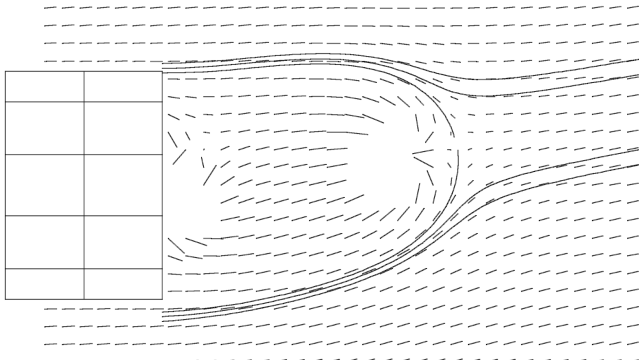
Fig. 2 Base flow velocity vectors and streamlines for the cone–cylinder at a 10 deg angle of attack.

Fig. 4 Pressures around the base of the cone–cylinder at a 10 deg angle of attack, with base pressure coefficient of −0.15 specified.

Fig. 5 Steady pressure distributions over the cone–cylinder at Mach 0.3.

wake shape is reasonable. As a starting point for these procedures, or if no fine tuning is to be done, the source should be placed one base diameter downstream of the base. The doublet can generally be located in the plane of the base.

In crossflow, the source should be displaced laterally to obtain a reasonable wake shape. A guideline is to displace the source by two-thirds of the crossflow component for a source position up to 1 base diameter downstream of the base, and by the full crossflow component for any additional distance downstream. This is illustrated in Fig. 2 for the cone–cylinder at a 10-deg angle of attack with the source placed 1 base diameter downstream of the base and with no base pressure specified.

The convergence of the iterative steady solution for the cone–cylinder at a 10-deg angle of attack is illustrated by plotting the pressures on the last segment of panels on the body. In the first case, shown in Fig. 3, the base pressure was not specified, and the iteration is hardly necessary. The zero-loading condition is enforced in an averaged sense: the pressure distribution in Fig. 3 is not constant, but the first harmonic component is zero. This is in contrast to the method of [9], in which the base pressure is applied to each panel around the circumference of the base. The base pressure coefficient dictated by the source position is approximately −0.1. It should be noted that the no-wake pressure distribution is not calculated as part of the iterative process and is only shown for reference. In the second case, shown in Fig. 4, a base pressure coefficient of −0.15, lower than that dictated by the source position, was specified. The iteration is clearly necessary in this case, but the convergence is rapid.

The behavior of the present method at the apex of the cone–cylinder is illustrated in Fig. 5 for Mach 0.3 at 9.5- and 10.5-deg angles of attack. The sharp increase in C_p toward the apex would at worst indicate a stagnation point at the apex and should not be interpreted as divergent behavior. It can be seen how the wake
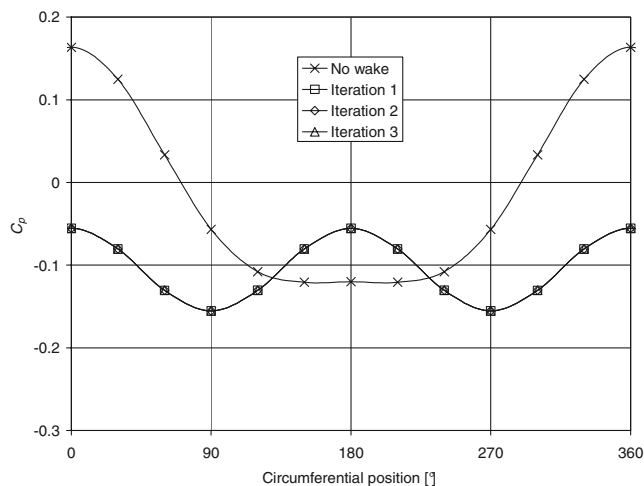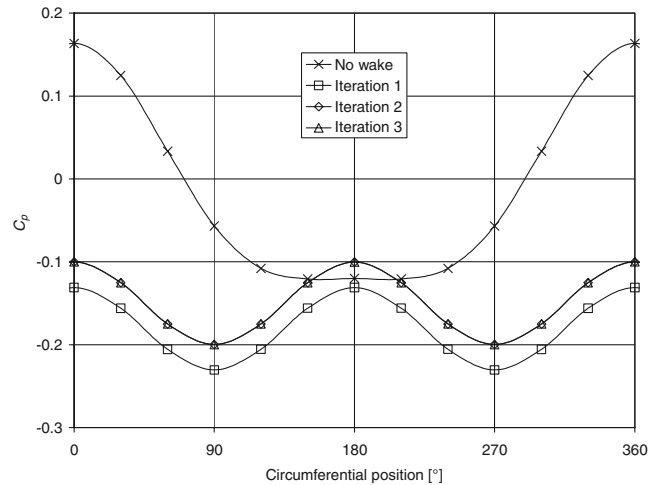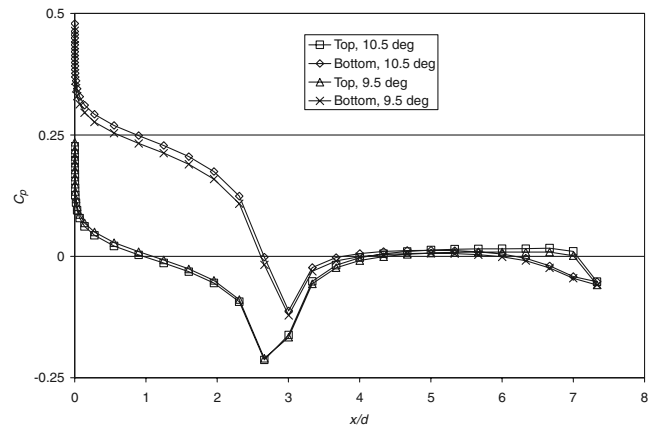
conditions result in practically equal pressures at the top and bottom of the rear of the body.

The consistency of the method with respect to the unsteady boundary conditions and pressure calculation was verified by comparing steady and quasi-steady pressure distributions over the cone–cylinder to unsteady pressure distributions for mode shapes that should result in the same pressure distributions. The incremental steady pressure distribution for a small change in angle of attack should be the same as the pressure distribution associated with a pitching mode around the same mean angle of attack at zero frequency, or a low-frequency plunging motion normal to the freestream. A plunging motion parallel to the freestream should result in an incremental pressure distribution that is proportional to the steady pressure distribution. In the results that follow, the base pressure was not specified and the source was placed one diameter downstream of the base and displaced laterally as shown in Fig. 2.

In Fig. 6 the quasi-steady results derived from the pressure distributions in Fig. 5 are compared with unsteady results for pitch and plunge modes at a mean angle of attack of 10 deg. The results are identical and well behaved at the apex. The large unsteady pressures at the top and bottom of the body rear end do not imply a large positive unsteady base pressure. The unsteady pressures at the sides of the body are of the opposite sign end even larger, resulting in a negative unsteady base pressure which is also consistent with the quasi-steady base pressure. The proper value for the unsteady base pressure is not known for this case, and seldom is in an aeroelastic analysis. Specifying a base pressure in this case would have forced the unsteady base pressure to zero, as would be the case with ZONA6, because there is no streamwise displacement of the base in either the pitch or plunge modes.
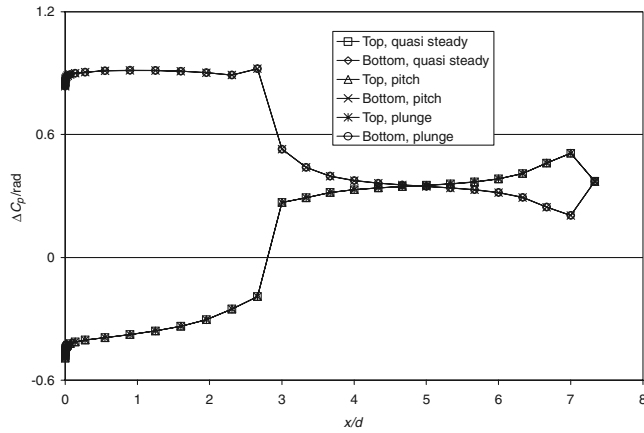

Fig. 3 Pressures around the base of the cone–cylinder at a 10 deg angle of attack, with base pressure not specified.

Fig. 6   Quasi-steady pressure distributions over the cone–cylinder at Mach 0.3 and 10 deg angle of attack for rotation and translation normal to the freestream.
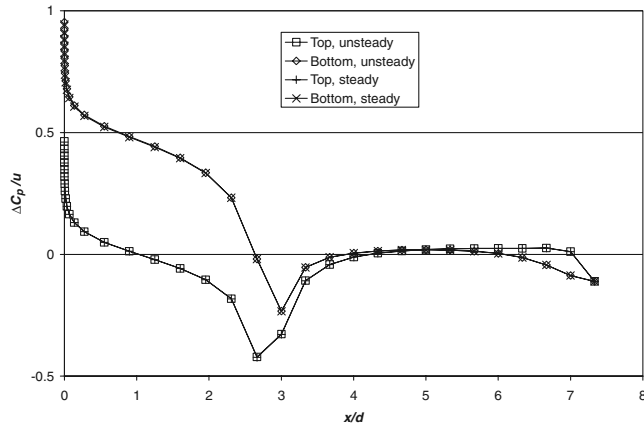

Fig. 8   Pitch-damping coefficient of a cone–cylinder body at Mach 0.3 for different pitch axis locations.

Fig. 7   Quasi-steady pressure distributions over the cone–cylinder at Mach 0.3 and 10 deg angle of attack for translation parallel to the freestream.

Fig. 9   NACA L51F07 wing–body combination showing the image system inside the body.

Fig. 10   Body normal load and wing pressure differential for the NACA L51F07 model at 4-deg angle of attack at Mach 0.6.

The change in steady pressure distribution associated with a change in velocity magnitude at a 10-deg angle of attack is compared with a low-frequency unsteady pressure distribution associated with a streamwise plunging motion in Fig. 7. Also in this case, the consistency between the unsteady and steady pressure distributions is confirmed. There is a significant unsteady base pressure, which is proportional to the steady base pressure. Specifying a base pressure in the present method would not force the unsteady base pressure to zero for this particular mode, whereas it would be forced to zero in ZONA6.

The steady base pressure coefficients at 9.5-, 10-, and 10.5-deg angles of attack were calculated as -0.103853, -0.105501, and -0.107227, respectively. From these values the quasi-steady base pressure coefficient for pitching was calculated as $-0.1933/\mathrm{rad}$ and exactly matched the unsteady low-frequency results for pitching and plunging normal to the freestream. The quasi-steady base pressure coefficient for streamwise plunging was calculated as 0.2110, whereas the corresponding unsteady, low frequency, result was 0.2104.

The calculated pitch-damping coefficient of the cone–cylinder for a range of pitch axis locations with and without a wake is shown in Fig. 8. The results with the wake model are in good agreement with the experimental results of [13] as well as with the ZONA6 results presented in [9] despite the different wake singularities used by the two analytical methods.

NACA Wing–Body Model L51F07

A two-strip image is used in the present method to model wing–body interference. The user specifies the y and z coordinates of the
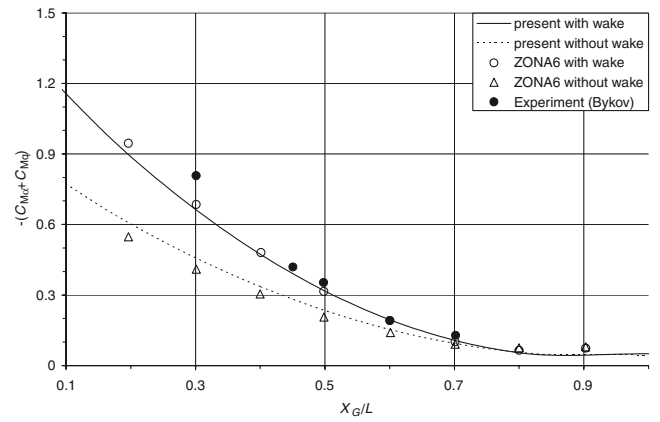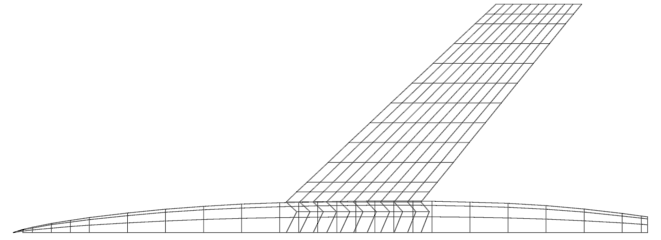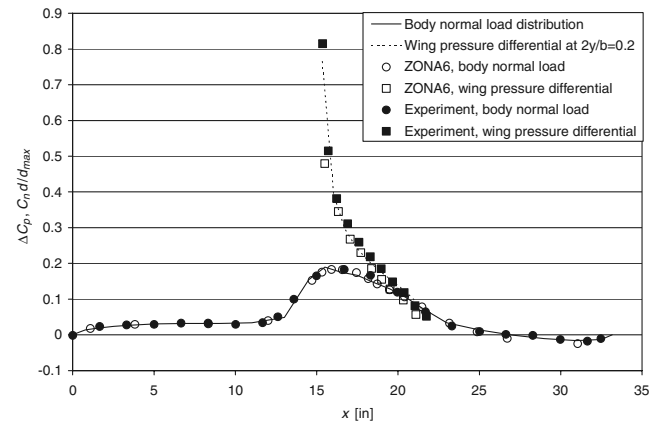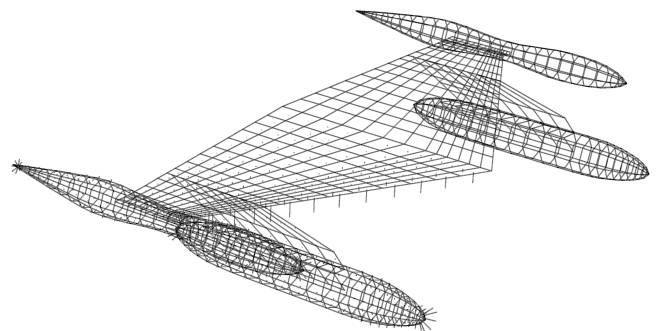

Fig. 11   NLR wing-tip tank-pylon-store model showing lifting surface panels, body surface panels, image panels, and steady pressures for Mach 0.45 and a zero angle of attack.

Table 1   Panel distributions

Element	Present	Roos et al. [5]	Chen et al. [9]
Wing	$13 \times 14 = 182$	$10 \times 9 = 90$	90
Tip tank	$25 \times 24 = 600$	$27 \times 8 = 216$	264
Pylon	$8 \times 2 = 16$	$10 \times 2 = 20$	24
Store	$24 \times 24 = 576$	$19 \times 8 = 152$	216
Total for wing-tip tank	782	306	354
Total for wing-tip tank-pylon-store model	1374	368	594

endpoints of the two image strips. The present code automatically assigns the x coordinates of the physical boxes to the image boxes in an alternating fashion. This results in a sawtooth appearance of the image within the body. The first image strip is intended to cancel the normal component of the induced velocity of the physical strip adjacent to the body, necessitating the reversal of the sweep angle between the physical strip and the first image strip. The second image strip is intended to move the trailing vortex to a convenient location (e.g., the body centerline). An example of the image system for the NACA L51F07 wing–body model of [14] is shown in Fig. 9. The steady normal loading on the body and the differential pressure distribution over the wing at $2y/b = 0.2$ for an angle of attack of 4 deg at Mach 0.6 are plotted in Fig. 10 and closely match the experimental data as well as the ZONA6 results of [9].

NLR Wing-Tip Tank-Pylon-Store Model

The NLR wing-tip tank-pylon-store model described in [15] approaches the complexity of real life applications of the present code. The present code includes some features that make it easier to deal with this complexity. The code produces an AutoCAD DXF (drawing interchange format or drawing exchange format) file for easy geometry checking using almost any 3-D CAD program. The DXF output shows the lifting surface panels, body surface panels, image panels (both in the symmetry plane and in bodies), normal vectors, steady flow velocity vectors, and steady pressures. A typical representation of the geometry and steady pressure distribution for a zero angle of attack at Mach 0.45 is shown in Fig. 11. Only the right-hand wing and stores were modeled; the left-hand side is composed of images generated by the code.

The calculation of unsteady pressures on body surfaces couples the steady and unsteady flowfields. The present code solves both the steady and the unsteady flowfields and therefore needs to provide a high fidelity steady solution. It is common to find cambered wing profiles and bodies that are not aligned with the global x axis. These features are not accounted for in the simplified aerodynamic models that are commonly used for aeroelastic analysis. The present code accounts for wing camber and store incidence angles in a simplified way. The lifting surface panels and body surface panels are not displaced from their idealized positions; only their normal vectors are rotated. The wing loading that is apparent in Fig. 11 is due to the

leading-edge droop of the profile. The stores are also set at small nose-down angles, but the resulting loads are too small to see from the picture.

The wing with stores was tested in two configurations, viz., wing with tip tank, and wing with tip tank, pylon, and store. A separated wake was not specified for the tip tank or the store in the present analysis to make a meaningful comparison to the NLR analytical results. All the ZONA6 results from [9] that are reproduced here are also the results without wakes. The analysis in [9] showed that the wake model had little influence on the steady pressure distribution on the tip tank. The analysis in [9] did show that flow separation on the store may have been significant; however, the effect on the unsteady pressure distributions on the store was not significant.

The paneling used in the present study is significantly finer than that used in [5,9]. The panel distributions are compared in Table 1. When available, the divisions are given as chord × span or axial × circumferential.

Steady pressure differential distributions at two spanwise stations over the wing in the wing with tip tank configuration are compared with the NLR experimental and analytical results [16] in Fig. 12. Station 3 is located at 48% of the nominal span and station 8 at 91.5% of the nominal span. The nominal span extends to the centerline of the tip tank. The loading is entirely due to the camber of the wing's leading edge and shows that the approximate scheme employed in the present method gives reasonable results.

Calculated steady pressures along two lines along the tip tank of the wing with tip tank configuration are compared with NLR experimental and analytical results [16] as well as ZONA6 results [9] in Fig. 13. These graphs show mostly the pressure distribution due to the body thickness distribution, except for the pressure peak corresponding to the leading-edge region of the wing on the inboard side. Both the present method and the NLRS method show this peak, but not ZONA6. Chen et al. [9] do not state explicitly whether the leading-edge droop of the profile, the sole source of the leading-edge pressure peak in the present results, was modeled.

In addition to the pressure peak at the wing's leading edge, the present results also show the effect of the trailing vortex. The wing's leading-edge droop and the setting angle of the tip tank result in a small downward lift force on the wing and a corresponding outward rotating trailing vortex emanating from the tail of the tip tank.
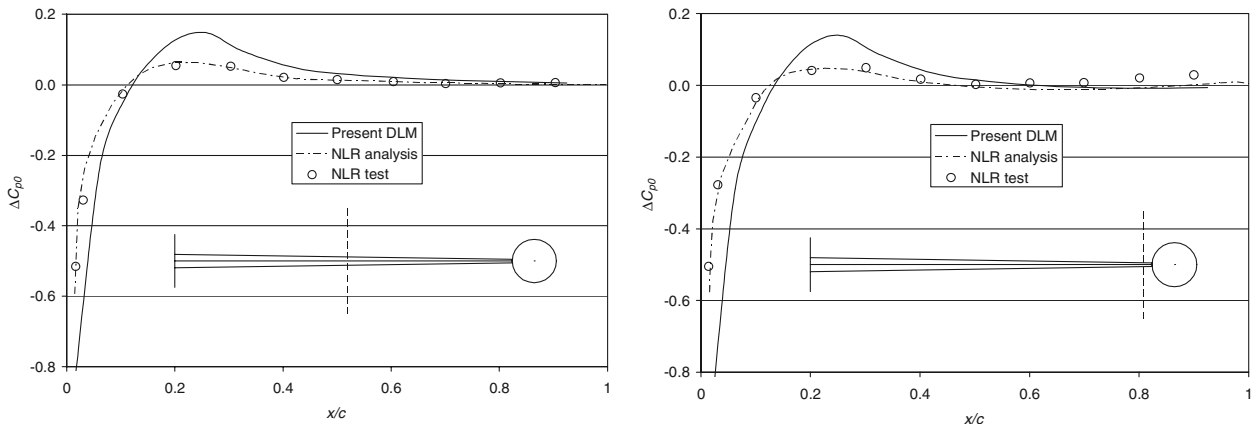

Fig. 12   Steady pressure differential over the wing of the wing-tip tank configuration at stations 3 and 8, at Mach 0.45 and with zero angle of attack.
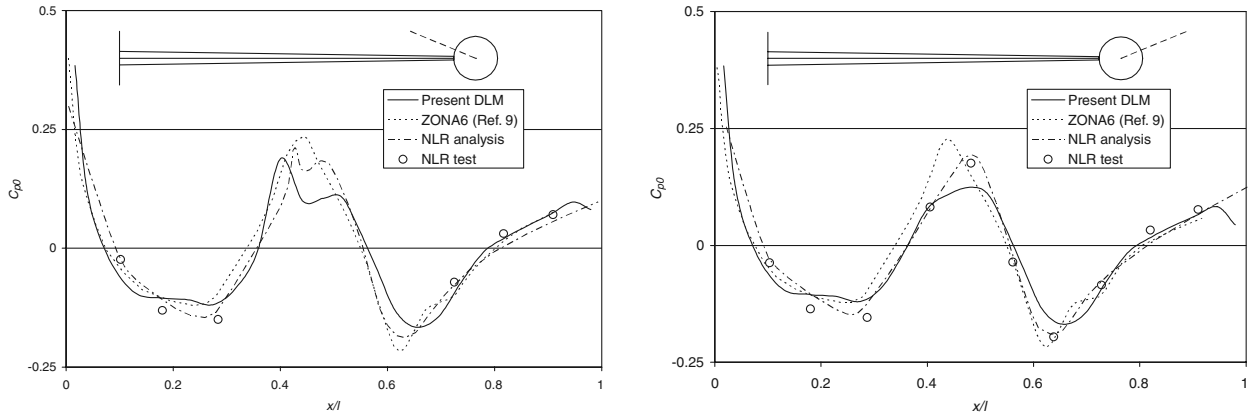
Fig. 13   Steady pressure distributions along the tip tank of the wing-tip tank configuration: inboard, 22.5 deg above the wing and outboard, 22.5 deg above the wing.

Toward the tail of the tank the tangential velocities approach infinity and there is a corresponding decrease in C_p, which can be seen in the present results toward the tail of the body. This is not evident in the NLRS results of [16], even though the leading-edge droop of the wing was modeled. In Fig. 14 the unsteady pressure distribution along the tip store at one circumferential position is compared with the NLR experimental and analytical results reported in [5] as well as ZONA6 results of [9]. There is reasonable agreement between all three analytical methods and the experimental results for the real part. In the imaginary part, the NLR analytical results are substantially different from the other analytical results. The magnitude of the

imaginary part is, however, much smaller than the magnitude of the real part. The apparently divergent behavior of the present results at the rear of the tank is due to the tip vortex of the wing. When the wing is pitched nose up, the positive lift on the wing results in an inward-rotating tip vortex emanating from the tail of the tip tank. Because this vortex is opposite to the steady vortex, it results in a decrease in tangential velocity and a corresponding increase in pressure, as can be seen in the real part of the present result. As the wing pitches up through the neutral position, the unsteady lift on the wing is still downward due to the lag of the circulation. The corresponding unsteady trailing vortex is therefore in the same direction as the
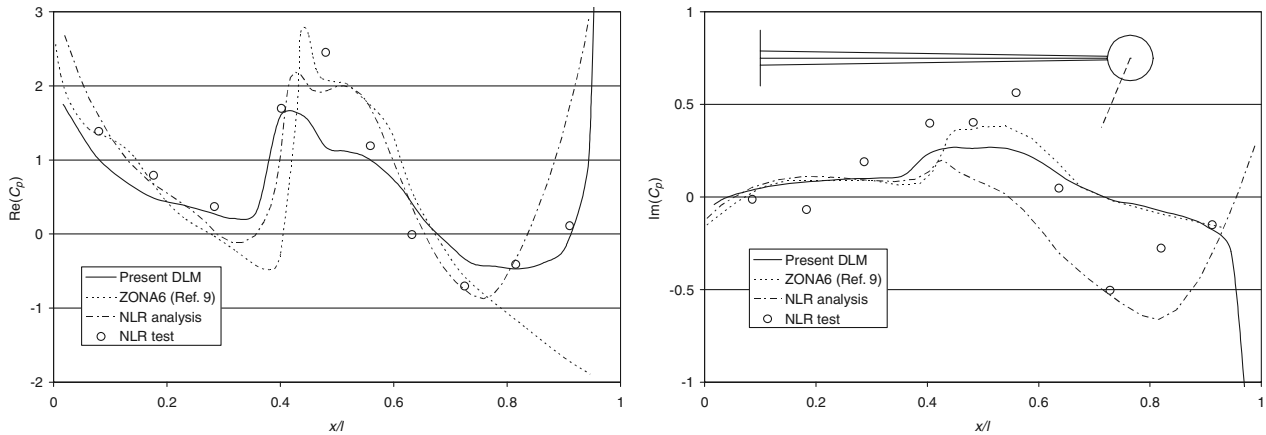

Fig. 14   Unsteady pressure distribution along the tip tank: inboard, 67.5 deg below the wing of the wing-tip tank configuration oscillating in a pitch mode.
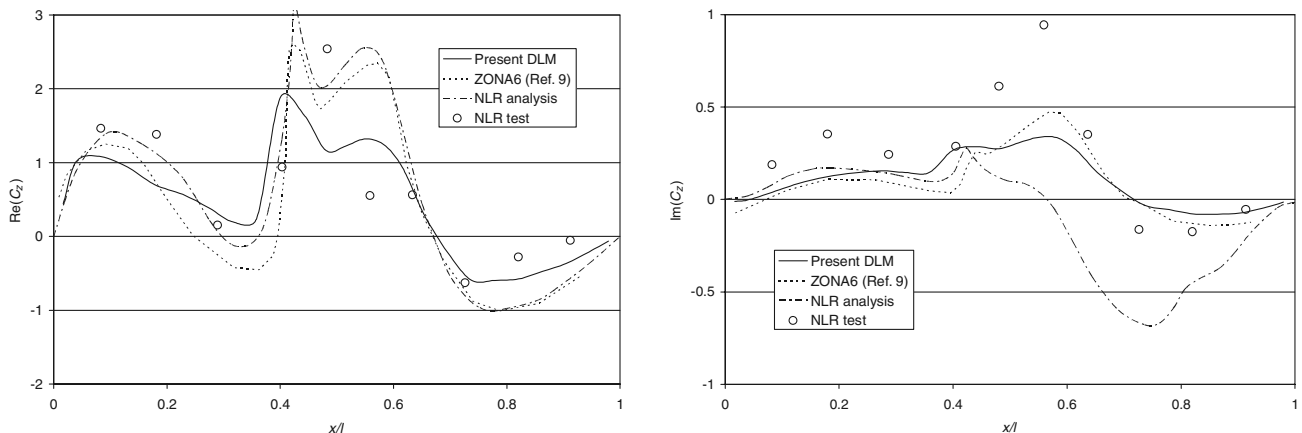

Fig. 15   Unsteady normal load distribution along the tip tank of the wing-tip tank configuration oscillating in a pitch mode.

steady trailing vortex, resulting in an increased tangential velocity and a decrease in pressure. This can be seen in the imaginary part of the present result.

This phenomenon is of little concern in the calculation of loads, because the area over which the excessively low pressures act is small, and the lateral load cancels on opposite sides of the body. There is generally good agreement between all the analytical and experimental results for the normal load distribution shown in Fig. 15 despite the differences in the pressure distributions over the

rear part of the tank. Also in this case, the imaginary part of the NLRI solution deviates substantially from the other analytical results.

Unsteady pressure distributions and the normal and side-load distributions on the store of the wing-tip tank-pylon-store configuration are compared with the NLR experimental and analytical results reported in [5] as well as ZONA6 results of [9] in Figs. 16–19. The agreement is generally good with the exception of the imaginary parts of the NLR analytical results.
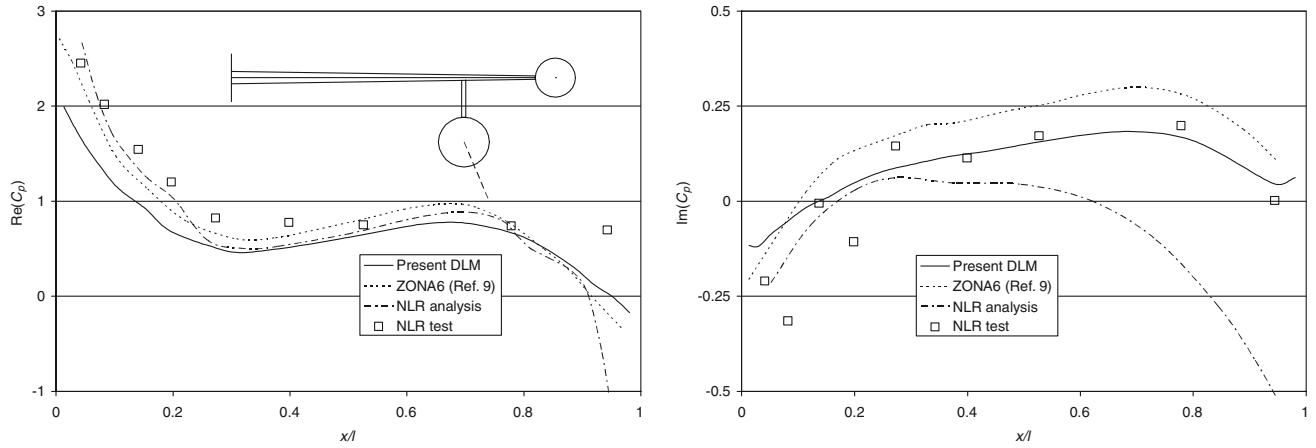

Fig. 16   Unsteady pressure distribution along the store: outboard, 157.5 deg from the top of the store of the wing-tip tank-pylon-store configuration oscillating in a pitch mode.
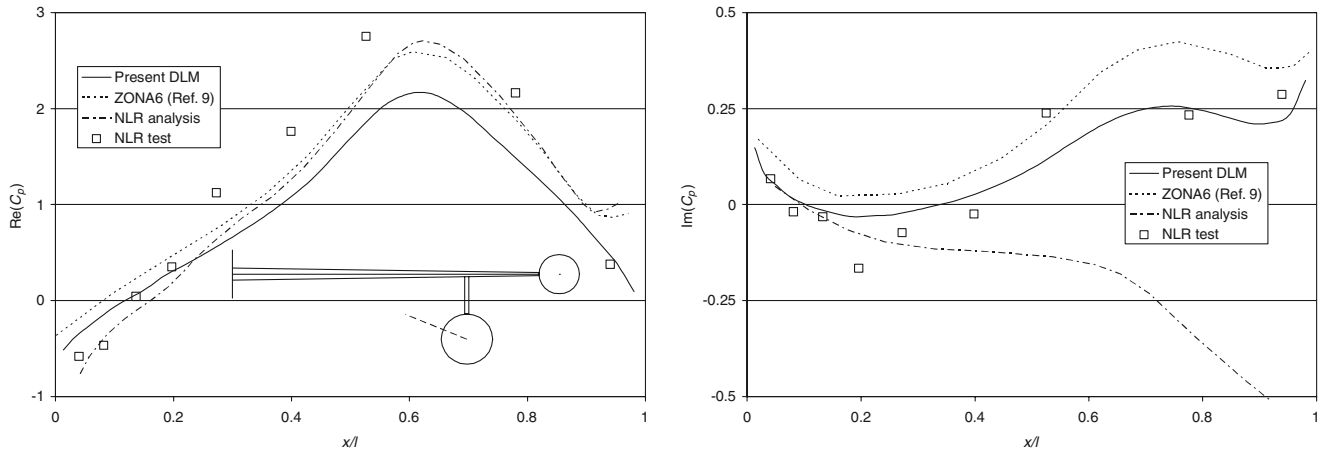

Fig. 17   Unsteady pressure distribution along the store: inboard, 67.5 deg from the top of the store of the wing-tip tank-pylon-store configuration oscillating in a pitch mode.
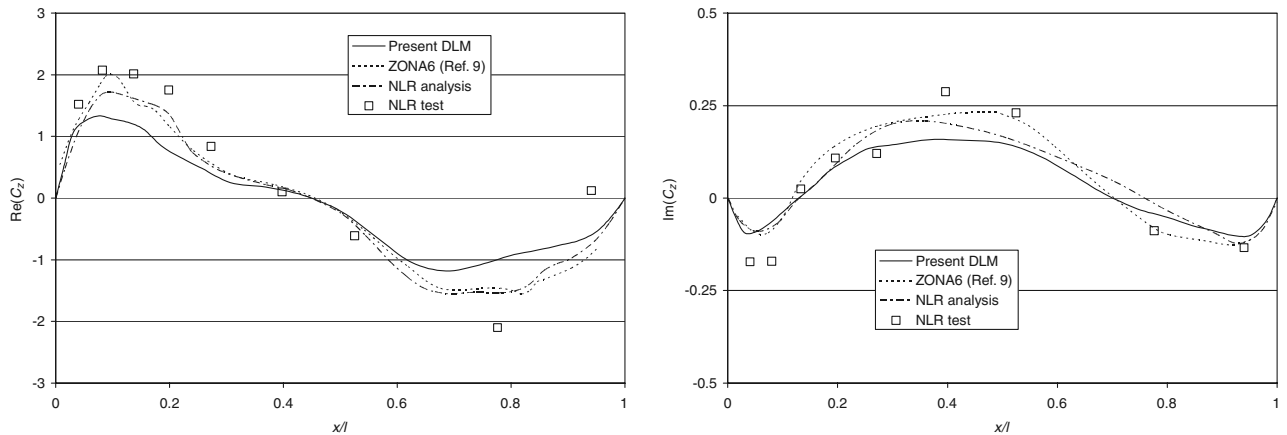

Fig. 18   Unsteady normal load distribution along the store of the wing-tip tank-pylon-store configuration oscillating in a pitch mode.
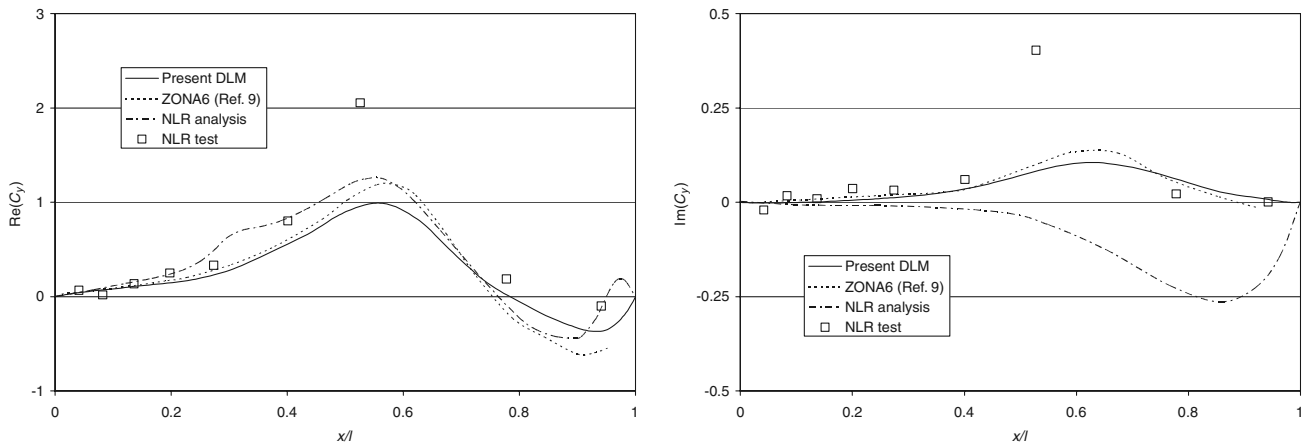
Fig. 19   Unsteady side load distribution along the store of the wing-tip tank-pylon-store configuration oscillating in a pitch mode.

Conclusions

A surface panel body model including a separated wake model was successfully implemented in the subsonic DLM. Compared with the popular implementations of the DLM, viz., the H7WC, N5KA, and N5KQ codes, it offers the advantage of more general body shapes that can be modeled using source panels on the body surface. Compared with the NLRI method developed three decades ago, which also used surface panels to represent bodies, it has the following advantages:

1) Simpler and consistent steady/unsteady flowfield coupling: it is not necessary to calculate higher derivatives of the steady disturbance velocity potential.

2) More sophisticated wing–body interference modeling: a two-strip image inside bodies instead of a single strip.

3) The separated wake model.

Compared with the ZONA6 code, which uses surface panels to represent bodies and offers a separated wake model, it has the following advantages:

1) The ability to calculate unsteady base pressures; this is applicable to blunt-base under-wing stores experiencing significant streamwise motion as well as blunt-based tip stores affected by the wing-tip trailing vortex.

2) Consistency between quasi-steady and unsteady results at zero frequency; in contrast to ZONA6, the present method uses compatible and colocated steady and unsteady wake singularities.

3) The simplicity and reliability of the DLM for lifting surfaces.

It is believed that the present development significantly enhances the capabilities of the subsonic DLM. The present computer code can be obtained from the author.

References

[1] Rodden, W. P., "The Development of the Doublet-Lattice Method," *Proceedings of the International Forum on Aeroelasticity and Structural Dynamics*, Vol. 2, Associazione Italiana di Aeronautica ed Astronautica, Rome, 1997, pp. 1–7.

[2] Giesing, J. P., Kálmán, T. P., and Rodden, W. P., "Subsonic Unsteady Aerodynamics for General Configurations: Part 1: Direct Application of the Nonplanar Doublet Lattice Method," U.S. Air Force Flight Dynamics Lab., Rept. AFFDL-TR-71-5, Dayton, OH, Nov. 1971.

[3] Giesing, J. P., Kálmán, T. P., and Rodden, W. P., "Subsonic Unsteady Aerodynamics for General Configurations, Part 2: Application of the Doublet-Lattice Method and the Method of Images to Lifting-Surface/Body Interference," U.S. Air Force Flight Dynamics Lab.,

Rept. AFFDL-TR-71-5, Dayton, OH, Apr. 1972.

[4] Rodden, W. P., Taylor, P. F., and McIntosh, S. C., Jr., "Further Refinement of the Nonplanar Aspects of the Doublet-Lattice Method," *Journal of Aircraft*, Vol. 35, No. 5, 1998, pp. 720–727.

[5] Roos, R., Bennekers, B., and Zwaan, R. J., "Calculation of Unsteady Subsonic Flow about Harmonically Oscillating Wing–Body Configurations," *Journal of Aircraft*, Vol. 14, No. 5, 1977, pp. 447–454.

[6] Hounjet, M. H. L., "ARSPNS: A Method to Calculate Steady and Unsteady Potential Flow About Fixed and Rotating Lifting and Non-Lifting Bodies," National Aerospace Lab./NLR TR 85114 U, Amsterdam, 1985.

[7] Hounjet, M. H. L., "ARSPNSC: A Method to Calculate Subsonic Steady and Unsteady Potential Flow About Complex Configurations," National Aerospace Lab./NLR TR 86122 U, Amsterdam, 1986.

[8] Hounjet, M. H. L., "CAR88: A Method to Calculate Subsonic and Supersonic, Steady and Unsteady, Potential Flow About Complex Configurations," National Aerospace Lab./NLR TR 88154 U, Amsterdam, 1988.

[9] Chen, P. C., Lee, H. W., and Liu, D. D., "Unsteady Subsonic Aerodynamics for Bodies and Wings with External Stores Including Wake Effect," *Journal of Aircraft*, Vol. 30, No. 5, 1993, pp. 618–628.

[10] Chen, P. C., Liu, D. D., and Sarhaddi, D., "High-Order vs Low-Order Panel Methods for Unsteady Subsonic Lifting Surfaces," *Journal of Aircraft*, Vol. 41, No. 4, 2004, pp. 957–959.

[11] Rodden, W. P., "Myth of the High-Order Lifting-Surface Method," *Journal of Aircraft*, Vol. 42, No. 2, 2005, p. 575.

[12] Van Zyl, L. H., "Surface Panel Body Model for the Subsonic DLM," *Proceedings of the International Forum on Aeroelasticity and Structural Dynamics*, Deutsche Gesellschaft für Luft- und Raumfahrt, Munich, 2005.

[13] Bykov, V. S., "Calculation of the Characteristics of Aerodynamic Damping of Bodies of Revolution," Foreign Technology Div., Air Force Systems Command, Rept. FTD-HT-23-1363-74, Wright–Patterson AFB, OH, June 1974.

[14] Loving, D. L., and Eastbrooks, B. B., "Transonic-Wing Investigation in the Langley 8-Foot High-Speed Tunnel at High Subsonic Mach Numbers and a Mach Number of 1.2," NACA RM L51F07, Sept. 1951.

[15] Renirie, L. T., "Analysis of Measured Aerodynamic Loads on an Oscillating Wing-Store Combination in Subsonic Flow," *Specialists Meeting on Wing-with-Stores Flutter*, CP-162, AGARD, Paper No. 5, Munich, 1974.

[16] Bennekers, B., Roos, R., and Zwaan, R. J., "Calculation of Aerodynamic Loads on Oscillating Wing/Store Combinations in Subsonic Flow," *Specialists Meeting on Wing-with-Stores Flutter*, CP-162, AGARD, Paper No. 4, Munich, 1974.